

Article

Cracking Behaviour of René 80-Type Superalloy During Laser-Based Directed Energy Deposition

Margarita Klimova ^{1,2,*}, Anastasiia Dmitrieva ¹, Rudolf Korsmik ¹, Grigoriy Zadykhan ¹, Ilya Astakhov ^{1,2}, Nikita Yurchenko ^{1,2}, Sergey Zherebtsov ^{1,2}, Nikita Stepanov ^{1,2} and Olga Klimova-Korsmik ¹

¹ World-Class Research Center, “Advanced Digital Technologies”, State Marine Technical University, 190121 Saint Petersburg, Russia; dmitrieva.av@ilwt.smtu.ru (A.D.); r.korsmik@ltc.ru (R.K.); g.zadykhan@ilwt.smtu.ru (G.Z.); astakhov@bsu.edu.ru (I.A.); yurchenko_nikita@bsu.edu.ru (N.Y.); zherebtsov@bsu.edu.ru (S.Z.); stepanov@bsu.edu.ru (N.S.); o.klimova@corp.smtu.ru (O.K.-K.)

² Laboratory of Bulk Nanostructured Materials, Belgorod State University, 308015 Belgorod, Russia

* Correspondence: klimova_mv@bsu.edu.ru

Abstract: Features of microstructure, mechanical properties, and cracking behaviour of the René 80-type superalloy manufactured by laser-based directed energy deposition (DED-LB) have been investigated. Different cracking behaviours were observed in two thin walls fabricated by DED-LB under different conditions. The defect-free thin wall was produced at low power and scanning speed, while increasing energy input during the process led to intensive cracking. Two types of cracks that developed in the René 80-type superalloy were identified: solidification hot cracking and ductility-dip cracking (DDC), caused by σ -phase particles. It was found that transition from an equiaxed structure to a columnar one increased the susceptibility to crack propagation.

Keywords: additive manufacturing; laser-based directed energy deposition; Ni-based superalloys; René 80; cracking



Citation: Klimova, M.; Dmitrieva, A.; Korsmik, R.; Zadykhan, G.; Astakhov, I.; Yurchenko, N.; Zherebtsov, S.; Stepanov, N.; Klimova-Korsmik, O. Cracking Behaviour of René 80-Type Superalloy During Laser-Based Directed Energy Deposition. *Metals* **2024**, *14*, 1434. <https://doi.org/10.3390/met14121434>

Academic Editor: Dariusz Rozumek

Received: 8 November 2024

Revised: 7 December 2024

Accepted: 10 December 2024

Published: 13 December 2024



Copyright: © 2024 by the authors. Licensee MDPI, Basel, Switzerland. This article is an open access article distributed under the terms and conditions of the Creative Commons Attribution (CC BY) license (<https://creativecommons.org/licenses/by/4.0/>).

1. Introduction

Ni-based superalloys are one of the most important classes of materials for aerospace and energy industries because of their superior performance at elevated temperatures. Due to high-temperature creep strength, fatigue, oxidation and corrosion resistance, Ni-based superalloys are widely used in the hot section of gas turbines [1,2]. For example, the René 80 (General Electric Company trademark) superalloy was developed in the 60 s for turbine engine components applications [3]. Nowadays, cast René 80 is widely used as a material for the first and second stage turbine blades operating at temperatures of 760–982 °C.

For producing engine parts of Ni-based superalloys, different conventional methods, such as casting [4], directional solidification [5,6], and powder metallurgy [7] are typically used. However, further thermomechanical processing (forging, rolling, extrusion, etc.) and complex machining (drilling, milling, cutting, etc.) are required for the fabrication of complex-shaped components with desired mechanical properties, which significantly increases the difficulty and cost of processing. Nowadays, one of the most relevant technologies that offers unique capabilities for production of components with complex geometry in a short production time is additive manufacturing (AM), which is also known as three-dimensional (3D) printing [8,9]. AM processes, based on powder bed fusion (PBF) or directed energy deposition (DED) are widely used for the production of metallic materials [10–13]. Among different DED technologies, powder-fed laser additive manufacturing, namely laser directed energy deposition (DED-LB), seems to be more attractive for nickel-based superalloys [13,14] due to an ability to fabricate large-scale components or repair critical parts with a proper surface quality.

Unique thermal history during AM processes includes repeated thermal cycles, very rapid heating and cooling rates, and large thermal gradients in melt pools. These non-

uniform conditions typically generate significant residual stresses, which intensify the cracking propensity in the deposited metal. Specifically, nickel-based superalloys containing a high fraction (>40–50 vol.%) of strengthening γ' phase $\text{Ni}_3(\text{Al,Ti})$ are highly susceptible to cracking during welding or AM [15,16]. It is believed that alloys (usually classified as “non-weldable”) with a content of Al + Ti more than 6.0 wt.%, demonstrate high levels of tensile residual stresses caused by rapid γ' precipitation [17]. Several cracking mechanisms were suggested to operate in superalloys produced by AM: solidification and liquation cracking (which requires the presence of a liquid phase); ductility-dip cracking (DDC), and strain-age cracking (SAC) (which occurs in the solid state) [18,19].

Thus, solving the cracking problem in nickel-based superalloys produced by AM is a key issue for both researchers and the industry. One of the most common approaches associated with the process is parameter optimisation. Many studies have shown that optimal parameters, which minimise crack formation, vary significantly depending on the exact AM process and printing materials [8,19]. Moreover, this approach may not work for some nickel alloys. Another promising way to improve the printability of Ni-based alloys is alloy design optimisation for AM [20,21]. In general, this approach is based on minimising the crystallisation range (difference between liquidus and solidus temperatures), which can lead to serious chemical heterogeneity [6,18]. Apparently, the addition of minor elements increases the solidification temperature range due to the segregation at grain boundaries and the formation of low-melting-point phases, which induces hot cracking during AM [22,23]. For example, Chauvet et al. detected the presence of boron-rich films in a Ni-Co-Cr-Mo-Al-Ti-B superalloy during electron beam melting (EBM) [24]; low-melting-point liquid films enriched in Zr and B in Inconel 738LC during selective laser melting (SLM) was observed by Cloots et al. [25].

It is well known that precipitation-hardened (30–50 vol.%) Ni-based “non-weldable” René 80 superalloy is severely susceptible to hot cracking [26,27]. The microstructure of René 80 consists of a γ matrix, typically strengthened by ordered, coherent intermetallic γ' — $\text{Ni}_3(\text{Al,Ti})$ precipitates, and intergranular $\text{M}_{23}\text{C}_6/\text{M}_6\text{C}$ and $\text{M}_5\text{B}_3/\text{M}_3\text{B}_2$ particles [28,29]. In the René 80 superalloy, borides decrease the grain boundary liquation temperature that leads to the development of extensive liquation cracking [30,31]. Osoba et al. reported that preventing the formation of borides, for example, via pre-weld heat treatment, resulted in a nearly crack-free heat-affected zone in laser-welded René 80 superalloy [32]. Therefore, in this work, decreasing the amount of C and removing B and Zr that strongly influence the crystallisation range was proposed to reduce the segregation of elements at grain boundaries, which should result in a decreased susceptibility to hot cracking. The aim of work was to demonstrate the possibility of fabrication of defect-free René 80-type superalloy by the DED-LB production, and to discuss the reasons that lead to an increase in cracking resistance.

2. Materials and Methods

René 80-type alloy powder without the addition of Zr and B, and with reduced carbon content was used as the raw material for fabrication by DED-LB. The powder was produced by the gas atomization method at Polema JSC (Tula, Russia). The actual composition (in wt.%) of the powder in comparison with René 80 (AMS-5403 standard) [33] is given in Table 1.

Table 1. Chemical composition of the René 80-type powder compared to the AMS-5403 standard (wt.%).

	Ni	Cr	Co	Mo	W	Ti	Al	Fe	Si	C	Zr	B
René 80-type	59.33	14.52	8.66	3.97	5.08	5.21	3.09	0.09	0.03	0.025	-	-
René 80 [33]	bal.	13.7–14.3	9.0–10.0	3.7–4.3	3.7–4.3	4.8–5.2	2.8–3.2	0–0.35	0–0.10	0.15–0.19	0.02–0.10	0.01–0.02

Powder characteristics, studied by SEM, are shown in Figure 1. The diameter and number of spherical particles were quantified using at least five SEM images. Powder particles were characterised by a predominantly spherical morphology with some satellites on the surface (Figure 1a). Some particles contained spherical pores, but their fraction was

less than 4% (Figure 1b). The particle size distribution in Figure 1c shows that particles are mostly 25–110 μm in size, with 1% of all particles being coarser (up to 230 μm). The average size of particles is 75 μm .

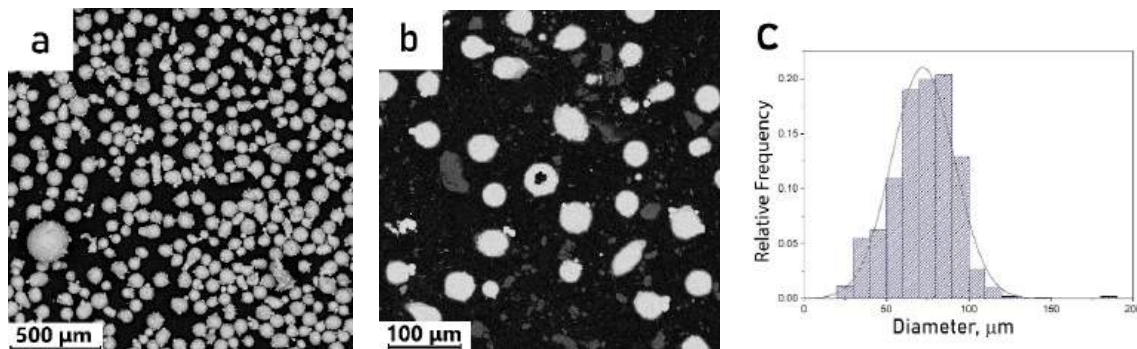


Figure 1. Powder characteristics: (a,b) particle morphology; (c) particle size distribution.

The thin walls were produced by DED-LB using an industrial robot LRM-200iD_7L (Fanuc, Oshino-mura, Japan) and an LS-3 Yb fibre laser (IPG Photonics, Oxford, MA, USA) with a maximum power of 3000 W. The laser welding head FLW D30 (IPG Photonics, Oxford, MA, USA) with a coaxial four-string SO12 nozzle (SPbSMTU, St. Petersburg, Russia) and Metco Twin 150 powder feeder (Oerlikon, Freienbach, Switzerland) were used for the powder supply. The samples were manufactured in a protective argon gas environment.

Thin walls with dimensions of $4 \times 30 \text{ mm}^2$ (mode 1) and $11 \times 50 \text{ mm}^2$ (mode 2) were fabricated on a steel substrate. The process was carried out at a low power of 200 W and a high power of 1800 W. Scanning speed was defined to evaluate different energy inputs (67 and 180 J/mm). Other parameters have been experimentally determined. The number of layers in both walls was 10. The process parameters are summarised in Table 2.

Table 2. DED-LB mode parameters.

Mode	Power, W	Scanning Speed, mm/s	Powder Feeding Speed, g/min	Laser Spot Size, mm	Height Offset, mm	Energy Input, J/mm
1	200	3	2.5	0.9	0.2	67
2	1800	10	15.8	2.5	0.6	180

The structure of thin walls was studied using optical metallography, scanning and transmission electron microscopy. The macrostructure was studied in longitudinal and transverse sections using an optical microscope—Leica DMi8 (Leica Microsystems, Wetzlar, Germany). For optical metallography, etching was carried out with a solution of acids HCl:HNO₃ at a ratio of 3:1. The microstructure of the deposited walls was studied using a scanning electron microscope (SEM)—Tescan MIRA3 LMH (Tescan, Brno, Czech Republic)—with an accelerating voltage of 20 kV, equipped with an Ultim Max 65 energy dispersive spectroscopy (EDS) detector and a C-Nano electron backscatter diffraction (EBSD) detector (Oxford Instruments NanoAnalysis, Abingdon, UK). EBSD images with a size of $2 \times 2 \text{ mm}^2$ were collected with a step size of 2 μm . Software AZtecAdvanced 6.0 and AZtecCrystal 2.2 (Oxford Instruments NanoAnalysis, Abingdon, UK) were used for analysis of the collected data. The samples for SEM observations were prepared by careful mechanical polishing using a Model 200 Dimpling Grinder (Thermo Fisher Scientific Inc., Waltham, MA, USA). In addition, a transmission electron microscope—Thermo Scientific™ Talos F200X G2 S/TEM—with a 4-segment EDX equipped with an energy dispersive spectrometry (EDS) detector (FEI Corporation, Hillsboro, OR, USA) was also used. Samples for SEM and TEM studies were cut in longitudinal sections from the middle of the walls and prepared using a Mill TEM Model 1051 ion sample thinning system (E.A. Fischione Instruments, Export, PA, USA). The fraction of pores, the grain size, and the size/fraction of

the particles were quantified using at least five optical, SEM and TEM images, respectively, using Digimizer software (version 6).

Mechanical properties were evaluated using a Future-Tech FM-310 micro Vickers hardness tester (Future-Tech Corp., Kawasaki, Japan) with a maximum load of 1 kg. Vickers microhardness tests were carried out with a 300 g load. At least 10 measurements per data point were made.

3. Results

The overall view and macrostructure of the René 80-type walls produced during DED-LB are shown in Figure 2. Although slight debonding of the deposited metal from the substrate occurred, no other visual defects were observed in the wall produced, according to mode 1 (Figure 2a). Contrary, in the wall produced by mode 2, a good metallurgical bond between the substrate and deposited metal did not lead to the formation of a defect-free structure: cracks propagated from the top to the bottom (Figure 2b).

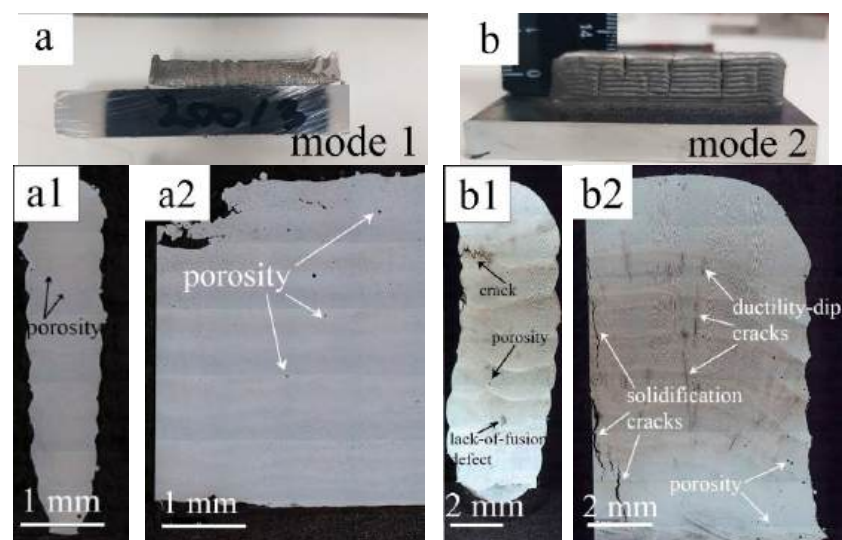


Figure 2. Overall view of (a) crack-free and (b) cracked walls; macrostructure in (a1,b1) transverse and (a2,b2) longitudinal sections.

The macrostructure of the crack-free wall in transverse and longitudinal sections (Figure 2(a1,a2)) was characterised by spherical porosity, especially near the top of the wall. A lack-of-fusion defects and extensive cracking were observed in another wall (Figure 2(b1,b2)). In addition, pores were located both at the top and near the substrate. The fraction of pores (0.25%) was higher compared to that (0.1%) of the crack-free wall.

A detailed identification of crack types was continued by an SEM investigation (Figure 3). The as-deposited wall had a dendritic structure with pronounced chemical heterogeneity. The equiaxed cellular structure was observed in the crack-free wall (Figure 3a). In turn, the structure of the cracked wall had an elongated dendritic morphology (Figure 3d). EDS maps (Figure 3b) showed the segregation of Ti in the interdendritic areas, whereas the cores of cells were enriched with Ni, Co, and Cr.

Two types of second-phase particles were observed in both walls by SEM. According to EDS analysis (Figure S1, Supplementary File), bright particles in Figure 3c,d were (Cr, Mo)-rich ones, and they had an average size of $\sim 1 \mu\text{m}$. In the crack-free wall, these particles were predominantly located on the cell boundaries, whereas in the cracked one, they were located on the elongated dendritic boundaries (Figure 3a compared with Figure 3d). This difference led to a change in volume fraction: $\sim 0.9\%$ and $\sim 0.5\%$ for the crack-free and cracked walls, respectively. Homogeneously distributed fine dark particles were mostly Ti-rich carbides (Figure 3c,f). The size ($\sim 0.2 \mu\text{m}$) and volume fraction ($\sim 0.4\%$) of the carbides were almost the same for both walls.

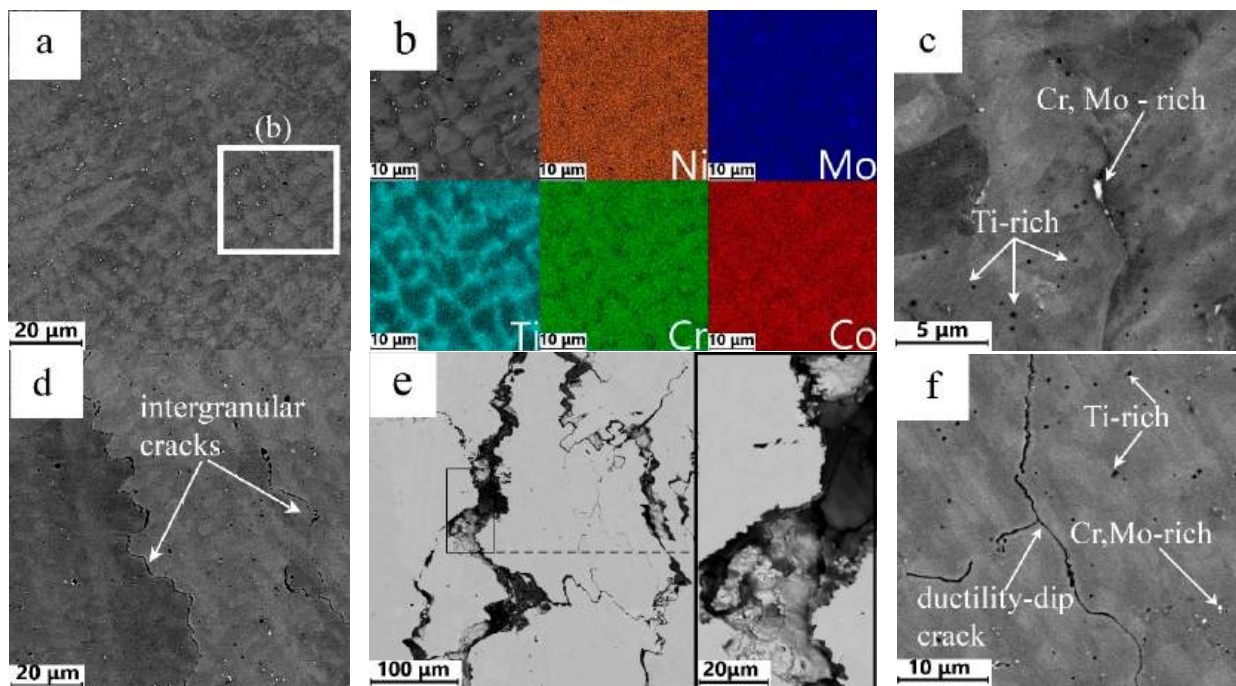


Figure 3. The SEM-BSE microstructure of (a–c) crack-free and (d–f) cracked walls in the longitudinal section; (b) energy-dispersive spectroscopy (EDS) elemental mapping of dendritic structure.

SEM investigations of the cracking behaviour of René 80-type superalloy after DED-LB indicated two operative cracking mechanisms. The primary cracks were caused by hot cracking, namely solidification cracking (Figure 3e). The crack growth occurred along interdendritic regions. Dendritic arms were visible inside the solidification crack. Another type of crack was associated with cracking in the solid state—ductility-dip cracking (Figure 3f). Fractured surfaces were straight and clean with sharp kinks. Cracks propagated along the grain boundaries; no primary γ - γ' eutectics or liquid films were detected.

EBSD analysis of the microstructure of the René 80-type walls in the centre of the longitudinal section is shown in Figure 4. The main difference between the walls was the grain morphology. The crack-free wall demonstrated a microstructural gradient from the bottom to the top of the sample (Figure 4a). Elongated grains that aligned with the laser movement path were observed near the substrate. The average grain thickness and length were about 35 μm and 150 μm , respectively. Nearly equiaxed fine grains with an average size of ~ 19 μm were formed higher along the cross section in the wall. In the cracked wall, the epitaxial grain growth along the building direction across several layers led to the formation of a coarse columnar structure (Figure 4b). EBSD analysis demonstrated that the crack propagation occurred along grain boundaries. Measured misorientation (Figure 4c) between the grains corresponding to the fractured surface showed that the crack propagated along the high-angle ($>15^\circ$) boundaries.

Detailed TEM studies of the alloy microstructure are presented in Figure 5. The fine structure of the crack-free wall (Figure 5a) consisted of the γ matrix and γ' precipitates. The volume fraction of γ' phase was relatively high ($\sim 55\%$), whereas the size of precipitates was very small—26 nm. Irregular (Cr, Co, Mo)-rich particles and (Ti, C)-rich particles were also found in the structure. Selected area electron diffraction (SAED) patterns allowed the identification of the (Cr, Co, Mo)-rich and (Ti, C)-rich particles as σ -phase and MC-types (TiC) carbides, respectively. In addition, the precipitation of (Al, O)-rich particles, which were deciphered as the Al_2O_3 oxides, occurred adjacent to carbides. Carbide and oxide precipitates adopted a “cube-on-cube” orientation relationship. The cracked wall had a qualitatively similar fine structure, but we observed the microcracks that initiated within σ -phase particles (Figure 5b).

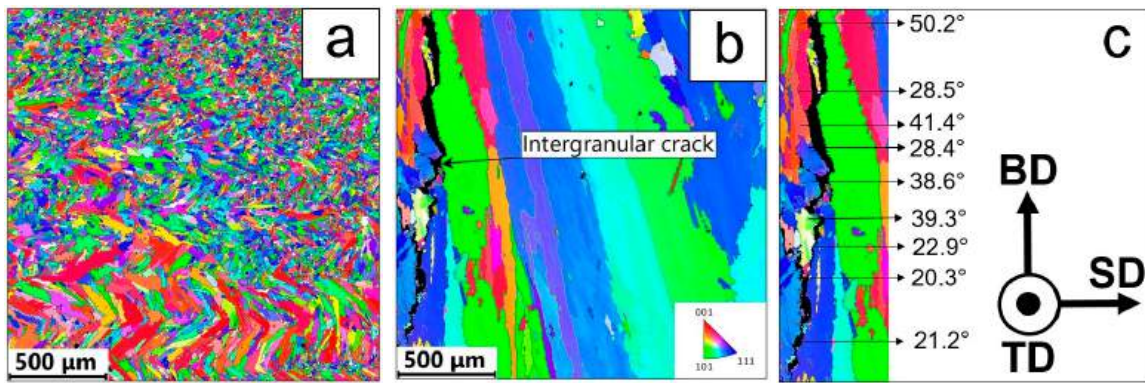


Figure 4. EBSD IPF images of (a) crack-free and (b) cracked walls in the longitudinal section; (c) the local misorientation between the grains near the crack. Here, BD—building direction, SD—scanning direction, TD—transverse direction.

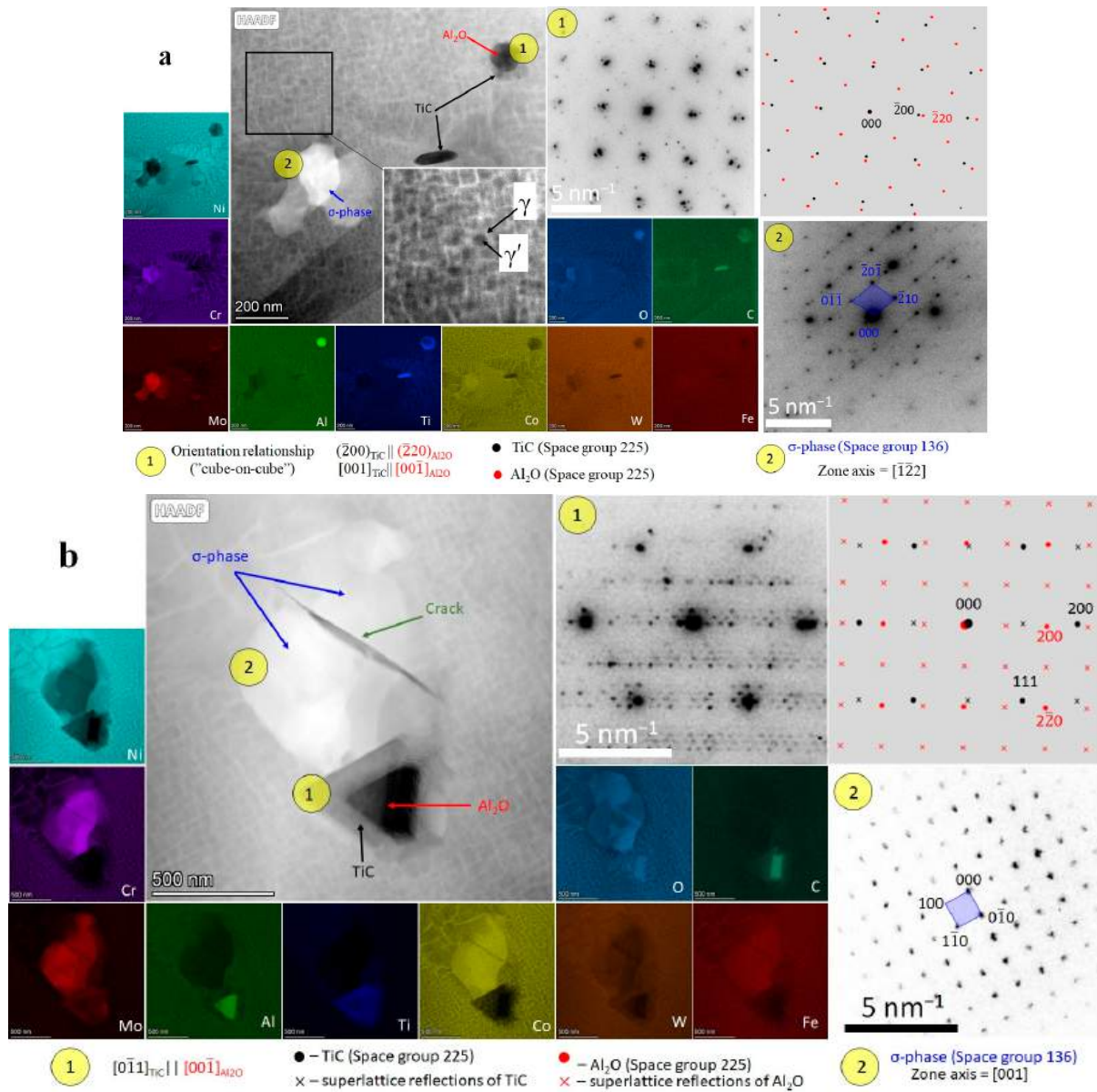


Figure 5. STEM-HAADF image of microstructure of (a) crack-free and (b) the cracked walls.

Figure 6 presents microhardness profiles from the bottom to the top of the walls. Both profiles showed a similar trend: a rapid increase in hardness from ~350–370 HV with elevating distance from the substrate, reaching an approximately constant value of ~510–540 HV (indicated by dotted lines). Slightly lower hardness in the cracked wall should be noted. Further, a gradual decrease in hardness in the top of the crack-free wall was most likely associated with the development of porosity. In turn, sudden drops in the hardness of the cracked wall were caused by the presence of microcracks in the indentation area.

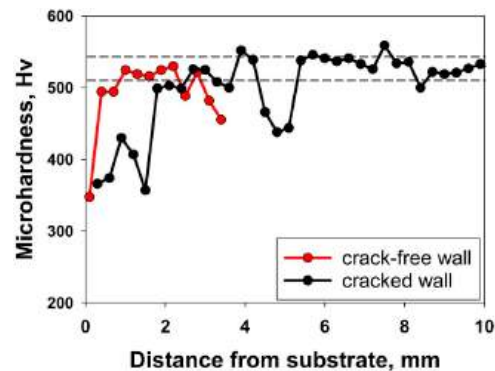


Figure 6. The microhardness profile in crack-free and cracked walls.

4. Discussion

In present work, the cracking behaviour of René 80-type superalloy thin walls fabricated by DED-LB under different process parameters was investigated. The reasons for crack formation depending on technological parameters, grain structure, and phase composition features will be discussed in detail.

The walls showed distinctively different behaviour: the wall fabricated at low power and scanning speed was nearly defect-free, while intensive cracking developed as these parameters increased (Table 2, Figure 2). The DED-LB process parameters significantly affect the microstructure characteristics such as residual stress, grain size, and types of precipitates via process temperature, which can lead to the different cracking behaviour [19]. For example, reduced susceptibility to cracking was observed at low laser powers with a small beam diameter or high powers with a large diameter in laser welded René 80 [26]. High power and low scanning speed caused an increment in the residual stress, which had a strong influence on crack resistance [34]. This finding was partially confirmed in [35]: minimisation of defects during SLM was ensured when both powers and speeds were high, or both were low. In general, with increasing heat input (in present work, 67 J/mm and 180 J/mm for mode 1 and mode 2, respectively), the tendency to cracking also increases [36]. Thus, although parameter optimisation seems to be a complex task factor, minimisation of laser power/beam diameter seems to be a promising strategy to produce crack-free specimens.

In addition to process parameters, the difference in the grain structure of the walls is one of the main features affecting crack formation and propagation. Nearly equiaxed structure was formed in the crack-free wall compared to the columnar structure in the cracked wall (Figure 4). The formation of columnar structures (Figure 4b) is quite typical during different AM processes [11,37]. Elongated grains have two growth directions, coinciding with the bidirectional movement of the laser. The average grain length (Figure 4a) corresponding to the laser height offset (Table 2) indicated that the grain growth was confined to one layer. One of the possible causes of the microstructure gradient is explained through the ratio of temperature gradient (G) to solidification rate (R) [38,39]. However, as was later suggested in [40], the structure formation during DED is more complex, depending on local fluctuations in G due to the Marangoni flow and in nucleation density due to the injected powder. In addition to differences in temperature gradient, which are greatly dependent on the size of the samples [41] (the crack-free wall has smaller dimensions compared to

the cracked one), changing the power of the process also has a strong impact on the grain morphology. The transition from the equiaxed structure to the coarse columnar one with increasing laser power has been previously noted in [42,43].

Hot cracking was observed in the René 80-type alloy in the present study, namely solidification cracking (Figure 3e), which is usually found in Ni-based superalloys obtained both by conventional and additive manufacturing [22,36]. In additively manufactured or welded metals, the complex heat history including repeated thermal cycles, rapid heating, and cooling rates, leads to the formation of dendritic structure. Molten metal at the melt pools solidifies under non-equilibrium conditions causing the segregation of elements. As dendrites grow, the islands of remaining liquid are formed in the interdendritic regions. With further solidification, liquid films formed in these areas under the influence of high residual stresses resulting from the shrinkage lead to the formation of cracks [44]. It is worth noting that element segregation was observed in both walls, but solidification cracking did not develop in the smaller wall. The second type of cracks observed in the alloy is associated with the ductility-dip cracking in the solid-state condition. In this work, it was found that the σ -phase could cause the initiation of DDC in René 80 alloy (Figure 5b). Microcracks, formed on the second phase particles, further propagate at high-angle grain boundaries (Figure 3f). Similar behaviour has been reported for Laves phase particles in the Thermo-Span superalloy [45]. DDCs usually propagate at long grain boundaries, since their gliding and migration at elevated temperatures are facilitated [46,47]. Although the fraction of grain boundaries decorated with σ -phase particles was higher in the crack-free wall (Figure 3a,d), it is obvious that the columnar structure, with long straight boundaries, provided more possibilities for fast crack propagation [48]. Meanwhile, equiaxed crystals are expected to have better crack resistance because tortuous boundaries effectively retard the propagation of cracks [49,50]. Additionally, EBSD analysis confirmed that cracks propagate mostly along the high-angle grain boundaries (misorientation angles more than 15°) (insert in Figure 4b), which is consistent with previous studies [24,51].

To rationalise the effect of chemical composition, equilibrium phase diagrams of the René 80-type alloy compared to the AMS-5403 standard (composition with Zr and B) were constructed using Thermo-Calc-2022b software, database TCHEA5: High Entropy Alloy v5.1 (Figure 7). The René 80-type alloy (Figure 7a) solidifies at 1210°C through the fcc phase matrix almost simultaneously with the formation of primary Ti-rich MC carbides. The solvus temperature of the ordered $L1_2$ phase (γ') was 1145°C . At a temperature of $\sim 1000^\circ\text{C}$, the precipitation of $M_{23}C_6$ -type instead of MC-type carbides is observed. Topologically close-packed (TCP) phases—(Cr, Mo)-rich σ -phase and (Cr, W)-rich μ -phase precipitate at $\sim 1100^\circ\text{C}$ and $\sim 850^\circ\text{C}$, respectively. Compared to the phase diagrams of “standard” René 80 (Figure 7b), René 80-type was predicted to have a higher solvus temperature and fraction of γ' and σ -phases, lower fraction of carbide phases, and no borides. Additionally, the solidification temperature range of the alloy was 105°C , which was 7°C lower than that of standard René 80. As mentioned above, formation and subsequent liquation of different types of borides on the grain boundaries is the main cause of hot cracking in René 80. The removal of elements, which are prone to segregation, leads to narrowing of the solidification interval and effectively prevents the development of liquation cracking.

The predicted diagram of the René 80-type alloy (Figure 7a) is in reasonable agreement with the observed experimental phase composition, except for the absence of $M_{23}C_6$ and μ -phases. The precipitation of M_6C or $M_{23}C_6$ types of carbides is observed in the “standard” René 80 alloy, although the presence of large primary MC carbides located on the grain boundaries was reported in [29,52]. However, during heat treatment or prolonged thermal exposure, primary carbides can decompose into $M_{23}C_6$ or (and) M_6C in accordance with the reaction of $MC + \gamma = M_{23}C_6/M_6C + \gamma'$ [53]. Apparently, nonequilibrium solidification during DED-LB leads to the precipitation of very fine, homogeneously distributed TiC carbides in the René 80-type alloy. In addition, small oxides were found. It seems that one type of particles (for example, oxides) serves as the preferred nucleation site for another (carbides), as suggested by Figure 5. Different types of oxides have also been observed

in nickel-based alloys produced by various additive technologies, as reported in [40,54]; moreover, in [51] oxides have been identified as the main cause of cracking during laser melting of Inconel 738. However, experimental observations of present study do not confirm the decisive role of oxides in cracking.

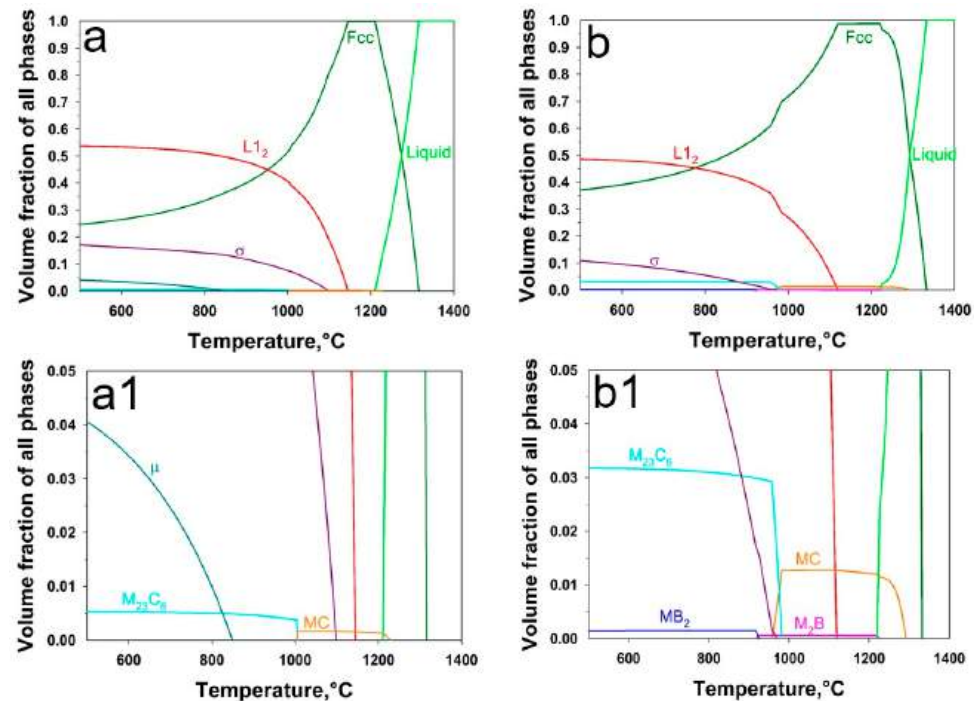


Figure 7. Equilibrium phase diagram of (a) the René 80-type and (b) the “standard” (AMS-5403) René 80 superalloys; (a1,b1) corresponding enlarged areas with a phase fraction of up to 0.05.

Instead, the findings of this study suggested cracking initiation at σ -phase precipitates (Figure 5b). Note that in the “standard” René 80 alloy, despite the Thermo-Calc predictions (Figure 7b), the precipitation of σ -phase is not typical, since the σ -forming elements, Cr and Mo, partition to borides [30]. However, according to the calculated phase diagram (Figure 7a), the René 80-type alloy is expected to be more susceptible to the σ -phase precipitation compared to the “standard” alloy. Yet, the fraction of σ -phase was significantly lower (less than 1% in present study) than expected (Figure 7a), possibly due to the non-equilibrium solidification conditions. Owing to the low symmetry of crystal structure, the σ -phase is known for its extreme brittleness [55]. Due to the difference in crystal structure and the lattice parameters of the σ -phase and γ -phase, the high stress field on the incoherent interface due to the lattice misfit can be generated. This may be one of the reasons for the reduction in high temperature mechanical properties of nickel superalloys [56]. However, the σ particles with plate-shaped morphology have orientation relationships with the matrix [57]. For example, OR corresponding to $(1-11)_{\gamma} // (00-1)_{\sigma}$ leads to the formation of two-atomic-layer steps on the incoherent interface, which provides the best lattices match of two distinct crystal structures [57,58]. In the present work, an increase in stresses at the interphase boundary is expected, since the observed morphology of the σ -precipitates was spherical and no orientation relationships between the matrix and the σ -phase were found. Therefore, crack initiation at these particles during AM fabrication is anticipated.

Despite the difference in grain structure morphology, changing DED-LB parameters do not have a noticeable effect on either the size or volume fraction of γ' particles, and, as a consequence, on the mechanical properties (Figures 5 and 6). It is well known that strength/microhardness of precipitation-hardened alloys is mainly determined by the size, morphology and fraction of the strengthening particles. The overall strength can be expressed as the sum of various contributions, such as precipitation strengthening,

solid solution strengthening, and grain boundary strengthening. For nickel-based superalloys the precipitation strengthening of the ordered γ' phase is the main strengthening mechanism [59]. Interaction between γ' particles and dislocations can be implemented through both bypassing and cutting; however, when the size of the γ' precipitates is small enough (~26 nm for both walls) precipitation strengthening operates according to weak pair-coupling mechanism. The critical resolved shear stress for the dislocation cutting by weakly coupled dislocation pairs [60]:

$$\Delta\tau_{wc} = 0.36 \left(\frac{\gamma_{APB}}{b} \right)^{3/2} \left(\frac{bd_{\gamma'} f_{\gamma'}}{\frac{Gb^2}{2}} \right)^{1/2} - 0.5 \left(\frac{\gamma_{APB}}{b} \right) f_{\gamma'} \quad (1)$$

where G is the shear modulus, b is the Burgers vector, $f_{\gamma'}$ and $d_{\gamma'}$ are volume fraction and size of the γ' phase, γ_{APB} is the anti-phase boundary energy.

In turn strengthening by non-shearable particles (for present work we mean carbides and σ -phase particles) is usually related to the Orowan mechanism of dislocation looping [61]:

$$\sigma_{Or} = \left(0.538 G b f^{0.5} d \right) \ln(d/2b) \quad (2)$$

here, f and d are the fraction and size of the carbides and σ -phase particles, respectively.

Solid solution strengthening is calculated as the hardening of dissolved elements in the γ matrix [62]:

$$\sigma_{ss} = f_{\gamma} \left[\sum_i \left(\beta_i^{\gamma} (x_i^{\gamma})^{1/2} \right)^2 \right]^{1/2} \quad (3)$$

where f_{γ} is the volume fraction of γ matrix, x_i^{γ} is the concentration of elements in the γ matrix, and β_i^{γ} is the solid solution strengthening coefficient of elements.

Grain boundary strengthening is represented by the Hall–Petch relationship [63]:

$$\sigma_{GB} = k_{HP} / \sqrt{D} \quad (4)$$

where k_{HP} is the Hall–Petch constant and D is the mean grain size.

Taking into account the same chemical composition and size/fraction of the second phases, contributions of the solid solution and precipitation strengthening will be the exactly same for both walls. Therefore, only grain boundary strengthening can cause the difference in the strength. Using Equation (4) with a Hall–Petch coefficient of 710 MPa $\mu\text{m}^{1/2}$ for nickel-based superalloys [64] and average grain sizes of ~19 μm for equiaxed structure and a transverse size of ~100 μm for columnar, the grain boundary strengthening will be ~160 MPa and ~70 MPa in crack-free and cracked walls, respectively. Thus, the difference in the yield strength of the alloy can be 90 MPa, which corresponds to ~27 Hv in accordance with the Tabor relationship [65].

Despite the insignificant difference depending on process parameters, in general, the microhardness of laser deposited René 80-type superalloy was significantly higher than that of the alloy obtained by other AM methods [20,66], conventional methods [52,67], or welding [68]. The increase in hardness was associated with the high-volume fraction of the strengthening γ' phase and rather than with the smaller grain size, which was found in the present work. It can be assumed that the strength of the superalloy will also be higher, but further studies are required to investigate the mechanical behaviour of the René 80-type superalloy, which was successfully produced by the DED-LB process.

5. Conclusions

In the present work, walls of René 80-type superalloy with reduced B, Zr, and C concentration were fabricated by DED-LB under different conditions. Phase composition, grain size, and morphology in deposited superalloy significantly influenced the cracking susceptibility. The reasons, leading to an increase in cracking resistance, namely (i) a

modification of the chemical composition in order to reduce the crystallisation range and (ii) the formation of the equiaxed structure under process with low-energy parameters; and the reasons leading to the development of different types of cracks were discussed in detail. The following conclusions have been drawn:

1. The crack-free wall was successfully fabricated using DED-LB at a low-energy process: power of 200 W, scanning speed of 3 mm/s, and laser spot size of 0.9 mm. Meanwhile, the increase in energy input (power of 1800 W and scanning speed of 10 mm/s) led to the development of solidification cracking.
2. The microstructure of the crack-free wall was represented mostly by fine equiaxed grains, while, in the cracked wall, coarse columnar grains were observed. Long, straight high-angle boundaries in the latter specimen provided an easy path for the crack growth.
3. The removal of B and Zr seemingly eliminated liquation cracking in the programme alloy due to reduced solidification range (as supposed by Thermo-Calc predictions). Yet, in the absence of borides, (Cr, Mo)-rich σ -phase precipitated—unusual for the René 80 superalloy. These σ -phase particles appeared to initiate the ductility-dip cracking.

Supplementary Materials: The following supporting information can be downloaded at: <https://www.mdpi.com/article/10.3390/met14121434/s1>. Figure S1: EDS elemental mapping of Rene 80-type structure.

Author Contributions: Conceptualization, M.K. and N.S.; methodology, R.K. and G.Z.; validation, R.K. and S.Z.; formal analysis, A.D., I.A. and N.Y.; investigation, G.Z., I.A. and N.Y.; resources, R.K. and G.Z.; data curation, M.K. and S.Z.; writing—original draft preparation, M.K.; writing—review and editing, S.Z. and N.S.; visualisation, A.D., I.A. and O.K.-K.; project administration, O.K.-K.; funding acquisition, N.S. All authors have read and agreed to the published version of the manuscript.

Funding: This research was funded by the Russian Science Foundation, grant no. 23-19-00622 (<https://rscf.ru/en/project/23-19-00622/>, accessed on 1 November 2024). A part of this research (microhardness measurements) was partially funded by the Ministry of Science and Higher Education of the Russian Federation as part of the World-Class Research Center program: Advanced Digital Technologies (Grant Agreement No. 075-15-2022-312, 20 April 2022).

Data Availability Statement: The original contributions presented in the study are included in the article/Supplementary Material, further inquiries can be directed to the corresponding author.

Conflicts of Interest: The authors declare no conflicts of interest.

References

1. Backman, D.G.; Williams, J.C. Advanced Materials for Aircraft Engine Applications. *Science* **1992**, *255*, 1082–1087. [[CrossRef](#)] [[PubMed](#)]
2. Unocic, R.R.; Viswanathan, G.B.; Sarosi, P.M.; Karthikeyan, S.; Li, J.; Mills, M.J. Mechanisms of creep deformation in polycrystalline Ni-base disk superalloys. *Mater. Sci. Eng. A* **2008**, *483–484*, 25–32. [[CrossRef](#)]
3. Earl, R. Cast Nickel Base Alloy. U.S. Patent US3615376A, 26 October 1971.
4. Zhang, J.; Singer, R.F. Effect of grain-boundary characteristics on castability of nickel-base superalloys. *Met. Mater. Trans. A* **2004**, *35*, 939–946. [[CrossRef](#)]
5. Zhang, J.; Singer, R.F. Hot tearing of nickel-based superalloys during directional solidification. *Acta Mater.* **2002**, *50*, 1869–1879. [[CrossRef](#)]
6. Grodzki, J.; Hartmann, N.; Rettig, R.; Affeldt, E.; Singer, R.F. Effect of B, Zr, and C on Hot Tearing of a Directionally Solidified Nickel-Based Superalloy. *Met. Mater. Trans. A* **2016**, *47*, 2914–2926. [[CrossRef](#)]
7. Jiang, J.; Yang, J.; Zhang, T.; Zou, J.; Wang, Y.; Dunne, F.P.E.; Britton, T.B. Microstructurally sensitive crack nucleation around inclusions in powder metallurgy nickel-based superalloys. *Acta Mater.* **2016**, *117*, 333–344. [[CrossRef](#)]
8. Bandyopadhyay, A.; Heer, B. Additive manufacturing of multi-material structures. *Mater. Sci. Eng. R Rep.* **2018**, *129*, 1–16. [[CrossRef](#)]
9. Gu, D.D.; Meiners, W.; Wissenbach, K.; Poprawe, R. Laser additive manufacturing of metallic components: Materials, processes and mechanisms. *Int. Mater. Rev.* **2012**, *57*, 3. [[CrossRef](#)]

10. Povolyaeva, E.; Astakhov, I.; Shaysultanov, D.; Klimova, M.; Zherebtsov, S.; Stepanov, N. Effect of thermo-mechanical treatment on cryogenic mechanical properties of a medium-entropy Fe65Co12.5Ni12.5Cr9.5Cu0.5 alloy produced by the laser-based powder bed fusion. *Mater. Sci. Eng. A* **2024**, *913*, 147059. [[CrossRef](#)]
11. Helmer, H.; Bauereiß, A.; Singer, R.F.; Körner, C. Grain structure evolution in Inconel 718 during selective electron beam melting. *Mater. Sci. Eng. A* **2016**, *668*, 180–187. [[CrossRef](#)]
12. Cunningham, C.R.; Flynn, J.M.; Shokrani, A.; Dhokia, V.; Newman, S.T. Strategies and processes for high quality wire arc additive manufacturing. *Addit. Manuf.* **2018**, *22*, 672–686. [[CrossRef](#)]
13. Yang, J.; Li, F.; Wang, Z.; Zeng, X. Cracking behavior and control of Rene 104 superalloy produced by direct laser fabrication. *J. Mater. Process. Technol.* **2015**, *225*, 229–239. [[CrossRef](#)]
14. Ramakrishnan, A.; Dinda, G.P. Direct laser metal deposition of Inconel 738. *Mater. Sci. Eng. A* **2019**, *740–741*, 1–13. [[CrossRef](#)]
15. Zhong, M.; Sun, H.; Liu, W.; Zhu, X.; He, J. Boundary liquation and interface cracking characterization in laser deposition of Inconel 738 on directionally solidified Ni-based superalloy. *Scr. Mater.* **2005**, *53*, 159–164. [[CrossRef](#)]
16. Tomus, D.; Rometsch, P.A.; Heilmaier, M.; Wu, X. Effect of minor alloying elements on crack-formation characteristics of Hastelloy-X manufactured by selective laser melting. *Addit. Manuf.* **2017**, *16*, 65–72. [[CrossRef](#)]
17. Henderson, M.B.; Arrell, D.; Larsson, R.; Heobel, M.; Marchant, G. Nickel based superalloy welding practices for industrial gas turbine applications. *Sci. Technol. Weld. Join.* **2004**, *9*, 13–21. [[CrossRef](#)]
18. Tang, Y.T.; Panwisawas, C.; Ghousoub, J.N.; Gong, Y.; Clark, J.W.G.; Németh, A.A.N.; McCartney, D.G.; Reed, R.C. Alloys-by-design: Application to new superalloys for additive manufacturing. *Acta Mater.* **2021**, *202*, 417–436. [[CrossRef](#)]
19. Mo, B.; Li, T.; Shi, F.; Deng, L.; Liu, W. Crack initiation and propagation within nickel-based high-temperature alloys during laser-based directed energy deposition: A review. *Opt. Laser Technol.* **2024**, *179*, 111327. [[CrossRef](#)]
20. Park, J.U.; Jun, S.Y.; Lee, B.H.; Jang, J.H.; Lee, B.S.; Lee, H.J.; Lee, J.H.; Hong, H.U. Alloy design of Ni-based superalloy with high γ' volume fraction suitable for additive manufacturing and its deformation behavior. *Addit. Manuf.* **2022**, *52*, 102680. [[CrossRef](#)]
21. Harrison, N.J.; Todd, I.; Mumtaz, K. Reduction of micro-cracking in nickel superalloys processed by Selective Laser Melting: A fundamental alloy design approach. *Acta Mater.* **2015**, *94*, 59–68. [[CrossRef](#)]
22. Heydari, D.; Fard, A.S.; Bakhshi, A.; Drezet, J.M. Hot tearing in polycrystalline Ni-based IN738LC superalloy: Influence of Zr content. *Mater. Process. Technol.* **2014**, *214*, 681–687. [[CrossRef](#)]
23. Ojo, O.A.; Richards, N.L.; Chaturvedi, M.C. Study of the fusion zone and heat-affected zone microstructures in tungsten inert gas-welded INCONEL 738LC superalloy. *Metall. Mater. Trans. A* **2006**, *37*, 421–433. [[CrossRef](#)]
24. Chauvet, E.; Kontis, P.; Jäggle, E.A.; Gault, B.; Raabe, D.; Tassin, C.; Blandin, J.J.; Dendievel, R.; Vayre, B.; Abed, S.; et al. Hot cracking mechanism affecting a non-weldable Ni-based superalloy produced by selective electron Beam Melting. *Acta Mater.* **2018**, *142*, 82–94. [[CrossRef](#)]
25. Cloots, M.; Uggowitzner, P.J.; Wegener, K. Investigations on the microstructure and crack formation of IN738LC samples processed by selective laser melting using Gaussian and doughnut profiles. *Mater. Des.* **2016**, *89*, 770–784. [[CrossRef](#)]
26. Rush, M.T.; Colegrove, P.A.; Zhang, Z.; Broad, D. Liquation and post-weld heat treatment cracking in Rene 80 laser repair welds. *J. Mater. Process. Technol.* **2012**, *212*, 188–197. [[CrossRef](#)]
27. Lim, L.C.; Yi, J.Z.; Liu, N. Mechanism of post-weld heat treatment cracking in Rene 80 nickel based superalloy. *Mater. Sci. Technol.* **2002**, *18*, 407–412. [[CrossRef](#)]
28. Shahsavari, H.A.; Kokabi, A.H.; Nategh, S. Effect of preweld microstructure on HAZ liquation cracking of Rene 80 superalloy. *Mater. Sci. Technol.* **2007**, *23*, 547–555. [[CrossRef](#)]
29. Safari, J.; Nategh, S. On the heat treatment of Rene-80 nickel-base superalloy. *J. Mater. Process. Technol.* **2006**, *176*, 240–250. [[CrossRef](#)]
30. Sidhu, R.K.; Ojo, O.A.; Chaturvedi, M.C. Sub-solidus melting of directionally solidified Rene 80 superalloy during solution heat treatment. *J. Mater. Sci.* **2008**, *43*, 3612–3617. [[CrossRef](#)]
31. Österle, W.; Krause, S.; Moelders, T.; Neidel, A.; Oder, G.; Völker, J. Influence of heat treatment on microstructure and hot crack susceptibility of laser-drilled turbine blades made from René 80. *Mater. Charact.* **2008**, *59*, 1564–1571. [[CrossRef](#)]
32. Osoba, L.O.; Sidhu, R.K.; Ojo, O.A. On preventing HAZ cracking in laser welded DS Rene 80 superalloy. *Mater. Sci. Technol.* **2011**, *27*, 897–902. [[CrossRef](#)]
33. AMS-5403A; Aerospace Material Specification. SAE International: Warrendale, PA, USA, 1984.
34. Huoa, Y.; Honga, C.; Li, H.; Liua, P. Influence of different Processing Parameter on distortion and Residual Stress of Inconel 718 Alloys Fabricated by Selective Laser Melting (SLM). *J. Mater. Res.* **2020**, *23*, e20200176. [[CrossRef](#)]
35. Wang, H.; Zhang, X.; Wang, G.B.; Shen, J.; Zhang, G.Q.; Li, Y.P.; Yan, M. Selective laser melting of the hard-to-weld IN738LC superalloy: Efforts to mitigate defects and the resultant microstructural and mechanical properties. *J. Alloys Compd.* **2019**, *807*, 151662. [[CrossRef](#)]
36. Chen, Y.; Zhang, K.; Huang, J.; Hosseini, S.R.E.; Li, Z. Characterization of heat affected zone liquation cracking in laser additive manufacturing of Inconel 718. *Mater. Des.* **2016**, *90*, 586–594. [[CrossRef](#)]
37. Liu, P.; Wang, Z.; Xiao, Y.; Horstemeyer, M.F.; Cui, X.; Chen, L. Insight into the mechanisms of columnar to equiaxed grain transition during metallic additive manufacturing. *Addit. Manuf.* **2019**, *26*, 22–29. [[CrossRef](#)]

38. Gäumann, M.; Bezençon, C.; Canalis, P.; Kurz, W. Single-crystal laser deposition of superalloys: Processing–microstructure maps. *Acta Mater.* **2001**, *49*, 1051–1062. [[CrossRef](#)]
39. Zhao, Y.; Koizumi, Y.; Aoyagi, K.; Wei, D.; Yamanaka, K.; Chiba, A. Molten pool behavior and effect of fluid flow on solidification conditions in selective electron beam melting (SEBM) of a biomedical Co–Cr–Mo alloy. *Addit. Manuf.* **2019**, *26*, 202–214. [[CrossRef](#)]
40. Pinkerton, A.J.; Karadge, M.; Syed, W.U.H.; Li, L. Thermal and microstructural aspects of the laser direct metal deposition of wasp alloy. *J. Laser Appl.* **2006**, *18*, 216–226. [[CrossRef](#)]
41. Dmitrieva, A.; Semenyuk, A.; Klimova, M.; Udin, I.; Mukin, D.; Vildanov, A.; Zherebtsov, S.; Klimova-Korsmik, O.; Stepanov, N. Cracking Behavior of the ZhS6K Superalloy during Direct Laser Deposition with Induction Heating. *Metals* **2024**, *14*, 610. [[CrossRef](#)]
42. Zhao, Y.; Aoyagi, K.; Yamanaka, K.; Chiba, A. A survey on basic influencing factors of solidified grain morphology during electron beam melting. *Mater. Des.* **2022**, *221*, 110927. [[CrossRef](#)]
43. Parimi, L.L.; Ravi, G.A.; Clark, D.; Attallah, M.M. Microstructural and texture development in direct laser fabricated IN718. *Mater. Charact.* **2014**, *89*, 102–111. [[CrossRef](#)]
44. Aucott, L.; Huang, D.; Dong, H.B.; Wen, S.W.; Marsden, J.; Rack, A.; Cocks, A.C.F. A Three-Stage Mechanistic Model for Solidification Cracking During Welding of Steel. *Metall. Mater. Trans. A* **2018**, *49*, 1674–1682. [[CrossRef](#)]
45. Yu, L.X.; Sun, W.R.; Zhang, Z.B.; Zhang, W.H.; Liu, F.; Qi, X.; Xin, F. The role of primary Laves phase on the crack initiation and propagation in Thermo-Span alloy. *Mater. Res. Innov.* **2005**, *19*, S68–S72. [[CrossRef](#)]
46. Fink, C. An investigation on ductility-dip cracking in the base metal heat-affected zone of wrought nickel base alloys—Part I: Metallurgical effects and cracking mechanism. *Weld. World* **2016**, *60*, 939–950. [[CrossRef](#)]
47. Collins, M.G.; Ramirez, A.J.; Lippold, J. An investigation of ductility-dip cracking in nickel-based weld metals—Part I. *Weld. J.* **2004**, *83*, 39–49.
48. Thompson, R.G. Microfissuring of Alloy 718 in the Weld Heat-Affected Zone. *JOM* **1988**, *40*, 44–48. [[CrossRef](#)]
49. Martin, J.H.; Yahata, B.D.; Hundley, J.M.; Mayer, J.A.; Schaedler, T.A.; Pollock, T.M. 3D printing of high-strength aluminium alloys. *Nature* **2017**, *549*, 365–369. [[CrossRef](#)]
50. Liu, Y.; Wu, D.; Gao, Z.; Gong, X.; Shao, Y.; Cao, Y.; Gao, Y.; Zou, Y. Influence of cold metal transfer welding parameters on the welding hot crack of Mar-M247 nickel-based superalloy. *J. Mater. Res. Technol.* **2024**, *30*, 6341–6354. [[CrossRef](#)]
51. Qiu, C.; Chen, H.; Liu, Q.; Yue, S.; Wang, H. On the solidification behaviour and cracking origin of a nickel-based superalloy during selective laser melting. *Mater. Charact.* **2019**, *148*, 330–344. [[CrossRef](#)]
52. Yang, C.; Xu, Y.; Nie, H.; Xiao, X.; Jia, G.; Shen, Z. Effects of heat treatments on the microstructure and mechanical properties of Rene 80. *Mater. Des.* **2013**, *43*, 66–73. [[CrossRef](#)]
53. Garosshen, T.J.; McCarthy, G.P. Low temperature carbide precipitation in a nickel base superalloy. *Metall. Mater. Trans. A* **1985**, *16*, 1213–1223. [[CrossRef](#)]
54. Guo, C.; Li, G.; Li, S.; Hu, X.; Lu, H.; Li, X.; Xu, Z.; Chen, Y.; Li, Q.; Lu, J.; et al. Additive manufacturing of Ni-based superalloys: Residual stress, mechanisms of crack formation and strategies for crack inhibition. *Nano Mater. Sci.* **2023**, *5*, 53–77. [[CrossRef](#)]
55. Hall, E.O.; Algie, S.H. The Sigma Phase. *Met. Rev.* **1966**, *11*, 61–88. [[CrossRef](#)]
56. Wang, C.; Wu, Y.; Guo, Y.; Guo, J.; Zhou, L. Precipitation Behavior of Sigma Phase and Its Influence on Mechanical Properties of a Ni-Fe Based Alloy. *J. Alloys Compd.* **2019**, *784*, 266–275. [[CrossRef](#)]
57. Sun, F.; Zhang, J.; Liu, P.; Feng, Q.; Han, X.; Mao, S. High Resolution Transmission Electron Microscopy Studies of σ Phase in Ni-Based Single Crystal Superalloys. *J. Alloys Compd.* **2012**, *536*, 80–84. [[CrossRef](#)]
58. Sengupta, S.; Krishnamurthy, H.R.; Ramakrishnan, T.V. A Microscopic Theory of the f.c.c.-b.c.c. Interface. *Europhys. Lett.* **1994**, *27*, 587–592. [[CrossRef](#)]
59. Goodfellow, A.J. Strengthening mechanisms in polycrystalline nickel-based superalloys. *Mater. Sci. Technol.* **2018**, *34*, 1793–1808. [[CrossRef](#)]
60. Xu, J.; Lin, X.; Guo, P.; Yang, H.; Xue, L.; Huang, W. The microstructure evolution and strengthening mechanism of a γ' -strengthening superalloy prepared by induction-assisted laser solid forming. *J. Alloys Compd.* **2019**, *780*, 461–475. [[CrossRef](#)]
61. Gladman, T. Precipitation hardening in metals. *Mater. Sci. Technol.* **1999**, *15*, 30–36. [[CrossRef](#)]
62. Wei, B.; Ji, H.; Guo, J. Effect of heat treatments on the microstructure and mechanical properties of René 104 superalloy manufactured by selective laser melting. *Mater. Charact.* **2023**, *200*, 112838. [[CrossRef](#)]
63. Hall, E.O. The Deformation and Ageing of Mild Steel: III Discussion of Results. *Proc. Phys. Soc. B* **1951**, *64*, 747–753. [[CrossRef](#)]
64. Galindo-Nava, E.I.; Connor, L.D.; Rae, C.M.F. On the prediction of the yield stress of unimodal and multimodal γ' Nickel-base superalloys. *Acta Mater.* **2015**, *98*, 377–390. [[CrossRef](#)]
65. Vela, B.; Khatamsaz, D.; Acemi, C.; Karaman, I.; Arróyave, R. Data-augmented modeling for yield strength of refractory high entropy alloys: A Bayesian approach. *Acta Mater.* **2023**, *261*, 119351. [[CrossRef](#)]
66. Acharya, R.; Bansal, R.; Gambone, J.J.; Kaplan, M.A.; Fuchs, G.E.; Rudawski, N.G.; Das, S. Additive Manufacturing and Characterization of René 80 Superalloy Processed Through Scanning Laser Epitaxy for Turbine Engine Hot-Section Component Repair. *Adv. Eng. Mater.* **2015**, *17*, 942–950. [[CrossRef](#)]

-
67. Barjesteh, M.M.; Abbasi, S.M.; Zangeneh, M.K.; Shirvani, K. The effect of heat treatment on characteristics of the gamma prime phase and hardness of the nickel-based superalloy Rene[®]80. *Mater. Chem. Phys.* **2019**, *227*, 46–55. [[CrossRef](#)]
 68. Sidhu, R.K.; Ojo, O.A.; Chaturvedi, M.C. Microstructural Response of Directionally Solidified René 80 Superalloy to Gas-Tungsten Arc Welding. *Met. Mater. Trans. A* **2009**, *40*, 150–162. [[CrossRef](#)]

Disclaimer/Publisher’s Note: The statements, opinions and data contained in all publications are solely those of the individual author(s) and contributor(s) and not of MDPI and/or the editor(s). MDPI and/or the editor(s) disclaim responsibility for any injury to people or property resulting from any ideas, methods, instructions or products referred to in the content.